Article:
Chong, G.S., Pope, S.A., Walker, S.N. et al. (2018) A statistical study of ionospheric boundary wave formation at Venus. Journal of Geophysical Research: Space Physics, 123 (9). pp. 7668-7685. ISSN: 0148-0227

https://doi.org/10.1029/2018JA025644

A statistical study of ionospheric boundary wave formation at Venus

Ghai Siung Chong[1], Simon A. Pope[1], Simon N. Walker[1], Rudy A. Frahm[2], Tielong Zhang[3,4], Yoshifumi Futaana[5]

[1]ACSE, University of Sheffield, Sheffield, UK.
[2]Southwest Research Institute, San Antonio, Texas, USA.
[3]Harbin Institute of Technology, Shenzhen, China.
[4]Space Research Institute, Austrian Academy of Sciences, Graz, Austria.
[5]Swedish Institute of Space Physics, Kiruna, Sweden.

Key Points:

- The ionospheric boundary is not always smooth. It is often observed to exhibit a wavelike appearance.
- Characteristics of the boundary wave are consistent with a Kelvin-Helmholtz Instability induced wave.
- Draping patterns of magnetic field lines set up favorable conditions for boundary wave excitation.

Corresponding author: Ghai Siung Chong, `gschong1@sheffield.ac.uk`

Abstract

Previous missions to Venus have revealed that encounters with plasma irregularities of atmospheric origin outside the atmosphere are not uncommon. A number of mechanisms have been proposed to discuss their origins as well as their roles in the atmospheric evolution of Venus. One such mechanism involves an ionopause with a wavelike appearance. By utilizing the magnetic field and plasma data from Venus Express (VEX), we present the first observational statistical analysis of the ionospheric boundary wave phenomena at Venus using data from 2006 to 2014. Results from the minimum variance analysis of all the photoelectron dropout events in the ionosphere reveal that the ionopause of Venus does not always appear to be smooth, but often exhibits a wavelike appearance. In the northern polar region of Venus, the normal directions of the rippled ionospheric boundary crossings lie mainly in the terminator plane with the largest component predominantly along the dawn-dusk (Y_{VSO}) direction. The average estimated wavelength of the boundary wave is 212 ± 12 km and the average estimated velocity difference across the ionopause is 104 ± 6 km/s. The results suggest that the rippled boundary is a result of Kelvin-Helmholtz Instability. Analysis reveals a correlation between the normal directions and the locations of the boundary wave with respect to Venus. This indicates the draping of magnetic field lines may play a role in enhancing the plasma flow along the dawn-dusk direction, which could subsequently set up a velocity shear that favors the excitation of ionospheric boundary wave by the KHI along the dawn-dusk direction.

1 Introduction

Due to the absence of an intrinsic magnetic field [*Russell et al.*, 1980; *Luhmann and Russell*, 1997], the solar wind interaction with Venus is highly dynamic. The Venusian ionopause, which is a boundary separating the shocked solar wind plasma and ionospheric plasma, is subjected to a number of plasma instabilities. The two main instabilities are the Rayleigh-Taylor Instability (RTI) (also known as the Interchange Instability [*Arshukova et al.*, 2004]) and the Kelvin-Helmholtz Instability (KHI). The Interchange Instability only grows when there is a non-monotonic plasma pressure gradient at the subsolar region [*Arshukova et al.*, 2004]. The KHI is a macroinstability that is principally generated by the strong shear flows across a boundary [*Chandrasekhar*, 1961] and is an important mode of energy transfer at Venus [*Futaana et al.*, 2017]. Important factors to the generation of KHI waves include the velocity, density and temperature gradients [*Amerstorfer et al.*, 2007;

Amerstorfer et al., 2010; *Ferrari et al.*, 1982; *Huba*, 1981; *Biernat et al.*, 2007; *Wolff et al.*, 1980; *Price*, 2008]. Even though the KHI is considered the more dominant instability for wave excitation, there are occasions when terms such as the magnetic field stress, gravity, and boundary curvature are more significant, and can give rise to other instabilities, for example the RTI or flute instability [*Elphic and Ershkovich*, 1984].

This wavelike appearance of the ionopause is an important characteristic of Venus and plays a significant role in its atmospheric evolution. For instance, when the Venusian ionospheric boundary is excited by the KHI, the boundary wave can grow, become nonlinear and subsequently reach a turbulent phase with non-regular structures [*Amerstorfer et al.*, 2010]. The vortices formed in the turbulent phase can eventually break up to create “atmospheric bubbles” (sometimes referred to as “plasma clouds”) [*Brace et al.*, 1982; *Wolff et al.*, 1980; *Thomas and Winske*, 1991]. These bubbles of atmospheric plasma will be convected downstream together with the solar wind bulk flow. At the same time, magnetic “flux ropes” [*Russell*, 1990] can also be formed and scattered within the ionosphere [*Wolff et al.*, 1980]. The estimation of the ion loss rate due to the convection of atmospheric bubbles is of the order of 10^{26} ions s^{-1} [*Brace et al.*, 1982; *Amerstorfer et al.*, 2010] which is higher than the rate of pick up $\approx 10^{25}$ ions s^{-1} [*Lammer et al.*, 2006] and sputtering processes $\approx 10^{24}$ ions s^{-1} [*Luhmann and Kozyra*, 1991]. It is widely accepted that the detachment of plasma clouds resulting from ionospheric boundary surface waves is one of the principal atmospheric loss processes at Venus [*Lammer et al.*, 2006; *Wolff et al.*, 1980; *Svedhem et al.*, 2007a; *Elphic et al.*, 1980]. Other atmospheric escape mechanisms operating at Venus include the thermal escape (or Jeans escape) [*Jeans*, 1955; *Chamberlain*, 1963], photo-dissociation [*McElroy et al.*, 1982; *Rodriguez et al.*, 1984], acceleration due to the J x B force [*Russell*, 1986] and ionospheric holes [*Hartle and Grebowsky*, 1993].

The concept of ionospheric boundary waves at Venus has long been studied in a number of model simulations. *Wolff et al.* [1980] showed that the ionospheric boundary is unstable to KHI and illustrated the formation of flux ropes and atmospheric bubbles as a result of the ionospheric surface wave. *Terada et al.* [2002] used a two-dimensional global hybrid model to investigate the KHI at Venus and showed that the ionopause in the subsolar region is unstable to KHI. *Biernat et al.* [2007] studied the growth of the KHI at the Venusian ionopause and found that KHI can evolve regardless of the solar wind conditions. *Amerstorfer et al.* [2010] and *Amerstorfer et al.* [2007] showed that a density increase can influence the growth rate of KHI and characterized the evolution of the KHI into three main phases, i.e. linear, nonlinear and turbulent phases. However, *Möstl et al.* [2011] showed that the ionopause is not able to reach the nonlinear vortex phase during either low or high solar activity due to the stabilizing density jump across the ionopause. In addition to Venus, the development of the KHI has been studied at other planets, including Mars [*Penz et al.*, 2004], Mercury [*Sundberg et al.*, 2010], Earth [*Nykyri and Otto*, 2001], Saturn [*Masters et al.*, 2009] and so on.

The continuous process of plasma loss resulting from ionospheric boundary wave events over a prolonged period of time plays a significant role in contributing to atmospheric loss at Venus. However, observational studies are rather limited and only short periods of Pioneer Venus Orbiter (PVO) data (one to two orbits of data) have been utilized. Using PVO data, *Luhmann* [1990] reported one of the earliest observations of an ionospheric boundary wave which is interpreted as the "terminator wave", based on the significant field behavior change within 15° of the terminator. The authors suggested a possible mechanism by the reverse orientation of the Interplanetary Magnetic Field (IMF) in the ionosphere and suggested its association with the formation of flux ropes. *Brace et al.* [1980] observed wavelike structures and interpreted them as PVO passing through the ionospheric surface wave, which can be due to the altitude changes of the Venusian ionopause. *Brace et al.* [1983] reported trans-terminator ionospheric waves into the nightside and suggested a potential wave energy by the plasma pressure gradient driven interchange instabilities or the ion-neutral drag driven shear instabilities. *Walker et al.* [2011] and *Pope et al.* [2009] suggested that nonlinear vortex-like structures observed in the magnetosheath region using Venus Express (VEX) magnetic field data were associated with the strong shear flow across the ionopause. However, the altitudes of these observations are not consistent with the nominal ionopause altitude. *Chong et al.* [2017] presented evidence for the ionospheric boundary exhibiting a wavelike appearance for a single VEX pass along the terminator.

To study the dynamics and characteristic distributions of the ionospheric boundary wave on Venus, a statistical analysis is conducted in this paper. Analysis of the available magnetic field and plasma data from the instruments on board of VEX from 2006 to 2014 reveals that the observations of such phenomena are not uncommon. Investigation of boundary wave formation is fundamental to our understanding of the atmospheric loss mechanisms operating and hence the atmospheric evolution of Venus and unmagnetized planets in general. The paper is structured as follows: The instrumentation is summarized in Section 2; The observations and data analysis of the ionospheric boundary wave are presented in Section 3; The characteristics of the boundary wave and its possible generation mechanisms are discussed in Section 4; The summary and conclusions are presented in Section 5.

2 Instrumentation: Venus Express

VEX had an elliptical polar orbit with periapsis ranging from 130 to 463 km at a latitude of about 78 °N. The apoapsis distance was around 66,000 km and VEX had an orbital period of 24 hours [*Titov et al.*, 2006; *Svedhem et al.*, 2007b]. The magnetic field was measured by the VEX Fluxgate Magnetometer (MAG) [*Zhang et al.*, 2006]. 1 Hz MAG data are used for the statistical analysis in this paper. These data have been cleaned to remove the dynamic stray fields [*Pope et al.*, 2011] and corrected for offset [*Leinweber et al.*, 2008]. The data have been rotated into the Venus Solar Orbital (VSO) coordinate frame; with $+X_{VSO}$ in the Venus-Sun direction, $+Y_{VSO}$ perpendicular to $+X_{VSO}$ and in the direction of the orbital motion of Venus, and $+Z_{VSO}$ is orthogonal to complete the right hand set of axes.

The electron spectrometer (ELS) and ion mass analyser (IMA) are part of the Analyser of Space Plasmas and Energetic Atoms (ASPERA-4) on board of VEX [*Barabash et al.*, 2007]. ELS provides electron energy spectra in several modes, two of which is used in this study: an electron spectrum between 0.9 eV to 15 keV is generated every 4 sec with an approximate energy resolution ($\Delta E/E$) of 7% (the energy resolution is energy and sector dependent) and an electron spectrum between 9 eV to 250 eV is generated every 1 sec with an approximate energy of 7%. The ion measurements provided by the IMA cover the energy range 0.01-36 keV/q with a sampling time of 192 seconds and an energy resolution ($\Delta E/E$) of 7%.

In contrast to PVO, which was able to sample the Venusian ionosphere in the subsolar region over the period of solar maximum, the high latitude elliptical polar orbit of VEX provides an opportunity to study the dynamics of the Venusian ionosphere in the northern polar region of Venus across nearly a full solar cycle with rather quiet solar activity [*Futaana et al.*, 2017].

3 Observations and data analysis

3.1 Photoelectron Dropouts

Figures 1 and 2 show the (a) VEX trajectory, (b) and (d) the electron energy-time spectrogram of differential energy flux, (c) and (f) the 1Hz magnetic field magnitude and (e) average electron energy flux at 22eV from VEX orbits on 08 Nov 2011 and 02 Oct 2011 respectively. Data in (e) is smoothed using a moving average filter of 7 data points. The location of the bow shock is highly variable due to the variations in the solar Extreme Ultraviolet (EUV), solar wind Mach number, and IMF orientation [*Zhang et al.*, 2008a]. Here the observed altitudes of the bow shock on both orbits are comparably different than the nominal bow shock locations [*Zhang et al.*, 2008a,b]. On the inbound leg of the orbit occurring on 08 Nov 2011, the bow shock was crossed at around 07:06 UT (at an altitude of 3395 km) with shocked solar wind appearing in the magnetosheath region around Venus. The broad energy intensity of these electron populations can be seen to become narrower towards the magnetic barrier at around 07:15 UT where the magnetic field magnitude increases until the inbound ionopause was crossed at around 07:18 UT. The ionosphere region is identified by the observation of the ionospheric photoelectron population at 21-24eV and at 27eV [*Coates et al.*, 2008; *Cui et al.*, 2011]. This can also be observed as an increase of the electron energy flux (averaged at ~22eV) in Figure 1(e). These photoelectron populations are mainly due to the photo-ionization of atmospheric oxygen by solar HeII 30.4 nm photons [*Coates et al.*, 2008]. VEX then crossed the ionopause and bow shock (not shown here) on its outbound pass, which can be similarly characterized as described above.

The VEX observations of the bow shock through to the magnetic barrier region on 02 Oct 2011 are similar to those on 08 Nov 2011. However, the behavior of the ionosphere on these two orbits are quite different. This is easily seen by comparing Figures 1(d) and 2(d). For instance, the ionospheric photoelectron population on 08 Nov 2011 is observed continuously within the ionosphere. In contrast, there were ten separate intervals when the ionospheric photoelectron population disappeared while VEX was in the ionosphere region on 02 Oct 2011. These will be termed "photoelectron dropout" events throughout this paper. These ten intervals of photoelectron dropouts can also be clearly reflected from the dips in the average electron energy flux at 22eV in Figure 2(e). The photoelectron dropout events on 02 Oct 2011 are not uncommon. After excluding the orbits where

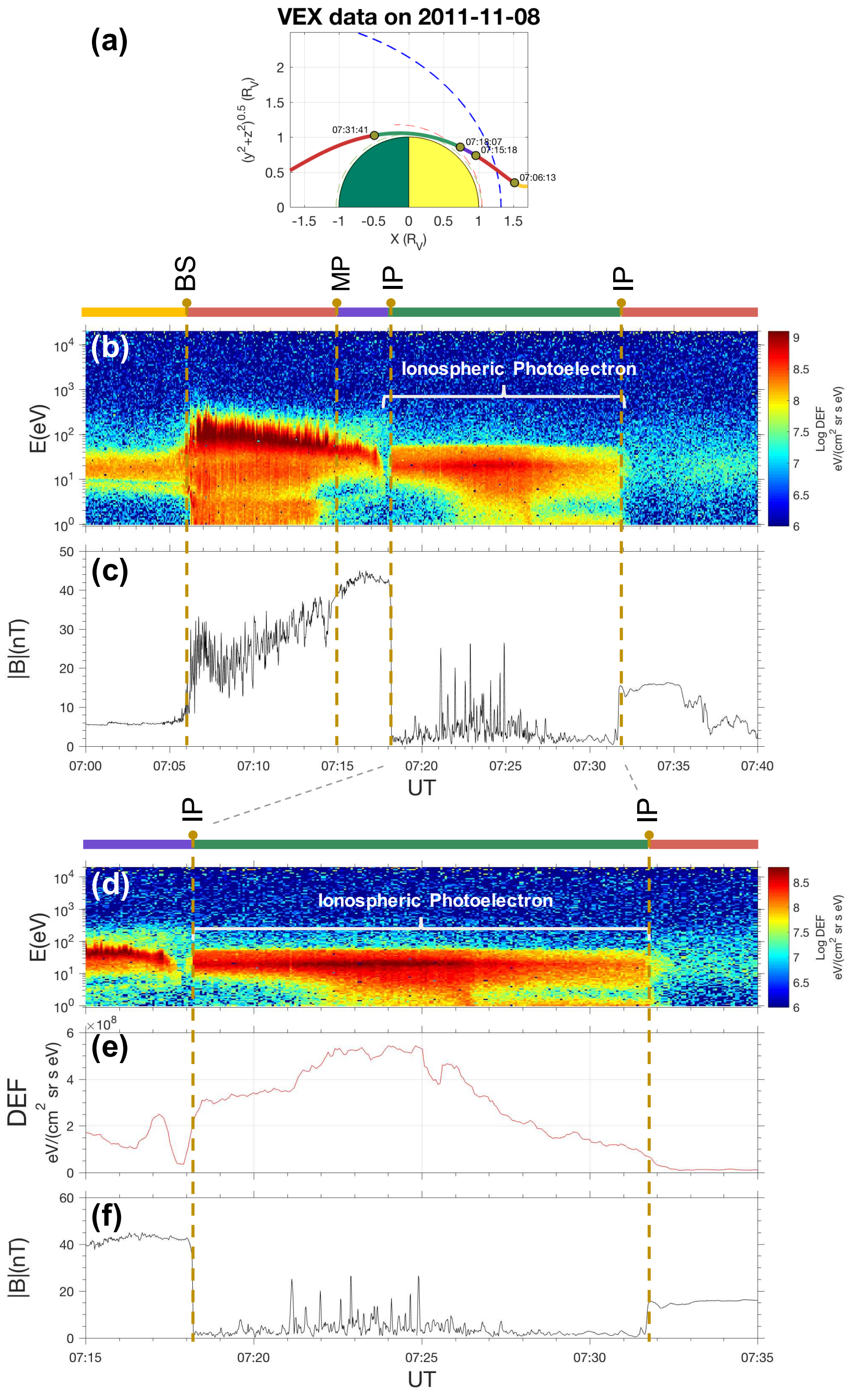

Figure 1. An example of the crossing of an unmagnetized ionosphere with continuous observations of ionospheric photoelectron population from 07:18 UT to 07:32 UT on 08 Nov 2011. (a) The VEX trajectory plot in R_V (Venus radii) which is colored in yellow, red, purple and green respectively to show the different regions (unshocked solar wind, magnetosheath, magnetic barrier and ionosphere) in which VEX was passing. These regions are also reflected by the colored bar above Figure 1(b) and (d). The nominal altitudes of bow shock (BS), induced magnetopause (MP) and ionopause (IP) represented using blue, red and green dashed lines respectively [*Zhang et al.*, 2008a,b] are plotted in (a). The actual crossings of the bow shock and ionopause are marked with golden circles and their respective times. (b) The electron energy-time spectrogram of differential energy flux and (c) 1-Hz magnetic field magnitude plots from 07:00 UT to 07:40 UT. Descriptions of (d) and (f) are same as (b) and (c) but from an expanded timescale 07:15 UT to 07:35 UT which focus mainly in the ionosphere region. (e) The average electron energy flux at 22eV (7-point smoothed).

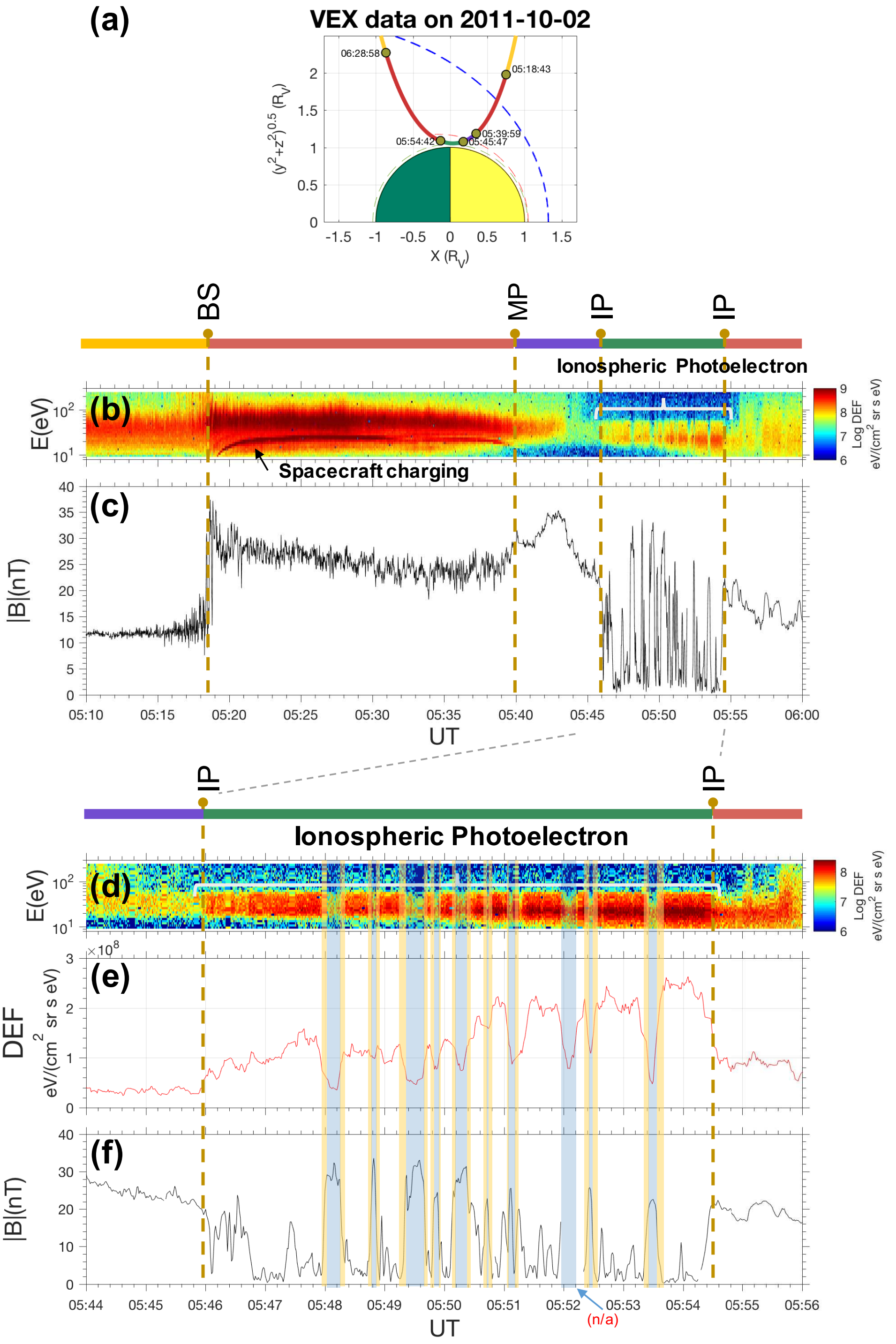

179 **Figure 2.** An example of an unmagnetized ionosphere perturbation with intervals of missing photoelectron
180 population ("photoelectron dropouts") while VEX was still within the inbound and outbound ionopause on 02
181 Oct 2011. Description of the figure has the same format as Figure 1 and the ionosphere perturbation is from
182 05:46:00 UT to 05:54:30 UT. All ten photoelectron dropouts are shaded in blue. There is missing magnetic
183 field data in the photoelectron dropout interval labeled "n/a". The yellow shaded regions correspond to the
184 dip-to-peak and peak-to-dip magnetic field fluctuations immediately adjacent to the photoelectron dropouts
185 regions.

the ELS and/or MAG data are unavailable when VEX was in the ionosphere, as well as orbits when ionospheric photoelectron populations are not observed at all, around 23% (495 orbits) show at least one or more intervals of photoelectron dropouts out of the remaining 2141 orbits from Apr 2006 to Nov 2014.

Throughout this study, the first observation of photoelectrons during an orbit is identified as the inbound ionopause crossing and the last observation of photoelectron population is identified as the crossing of the outbound ionopause. The ionosphere is the region between the inbound and outbound ionopause.

It can be seen from Figure 2 (apart from one interval labeled “n/a” which is associated with a gap in magnetic field data and which will be omitted from the following analysis), each of the nine blue-shaded photoelectron dropout intervals on 02 Oct 2011 correspond to an increase in the magnetic field magnitude. Compared to the ionospheric regions of low field magnitude, the larger magnetic field magnitude regions are comparable to that observed in the magnetic barrier region just before the first ionopause crossing. In addition, the electron energy intensity during the photoelectron dropout intervals are also comparable to the intensity in the magnetic barrier region as seen from Figure 2(d) and (e). Note that for the purposes of readability, the plot of average energy flux in Figure 2(e) is 7-point smoothed. As a result, the presented energy fluxes of a couple of photoelectron dropout intervals appear to be larger than the flux intensity in the magnetic barrier.

The occurrence of the photoelectron dropouts implies that while VEX was in the ionosphere (where ionospheric photoelectron population should be constantly observed), there were periods when VEX detected electron population similar to those in the magnetic barrier region. However, to travel from the magnetic barrier to the ionosphere region or vice versa, VEX would be expected to cross the ionopause.

3.2 Ionospheric boundaries crossings

To assess if these photoelectron dropout events on 02 Oct 2011 relate to ionopause crossings all of the 18 (yellow-shaded) regions adjacent to the periods in which photoelectron dropout events were observed were investigated using Minimum Variance (MV) analysis [*Sonnerup and Scheible*, 1998]. MV analysis is implemented over the dip-to-peak and peak-to-dip field fluctuations to determine if they are ionopause crossings. In the case that they are boundary crossings, MV analysis is used to find the boundary normal directions.

Table 1. A summary of the results of the Minimum Variance Analysis applied to the Venus Express data from 02 Oct 2011 for all the photoelectron dropout intervals shown in Figure 2.

Time (UT)		MV Direction							
From	To	X	Y	Z	$\lambda_{int}/\lambda_{min}$	$\lvert B_n\rvert/\lvert B\rvert$	$\lvert\triangle B\rvert/\lvert B\rvert$	$\theta_{B_n\_B}$ (deg)	Data Point
‘05:47:56’	‘05:48:03’	0.187	0.979	0.081	23.04	0.00	0.92	89.8	8
‘05:48:15’	‘05:48:21’	0.070	0.574	-0.816	5.07	0.01	0.74	89.3	7
‘05:48:42’	‘05:48:49’	0.096	0.956	-0.276	42.67	0.07	0.93	86.0	8
‘05:48:49’	‘05:48:55’	0.066	0.986	-0.156	1305.10	0.06	0.89	86.7	7
‘05:49:15’	‘05:49:22’	0.207	0.882	0.423	18.97	0.01	0.95	89.4	8
‘05:49:35’	‘05:49:42’	0.012	-0.607	0.795	10.54	0.01	0.68	89.6	8
‘05:49:47’	‘05:49:50’	0.369	0.868	-0.333	8.66	0.05	0.92	87.3	4
‘05:49:53’	‘05:50:50’	0.109	0.868	-0.485	92.38	0.14	0.89	82.2	8
‘05:50:04’	‘05:50:11’	0.142	0.942	0.303	34.09	0.00	0.93	89.8	8
‘05:50:22’	‘05:50:36’	0.177	0.866	-0.469	4.26	0.09	0.79	85.1	15
‘05:50:37’	‘05:50:42’	0.047	0.738	-0.674	50.77	0.14	0.89	81.8	6
‘05:50:43’	‘05:50:48’	0.070	0.989	0.129	10.01	0.10	0.63	84.2	6
‘05:50:55’	‘05:50:59’	0.324	0.839	0.438	32.14	0.12	0.86	83.3	5
‘05:51:07’	‘05:51:11’	0.111	0.960	0.258	31.27	0.10	0.76	84.2	5
‘05:52:20’	‘05:52:25’	0.083	0.778	-0.622	46.53	0.07	0.87	85.8	6
‘05:52:27’	‘05:52:34’	0.096	0.551	-0.829	3.50	0.02	0.91	89.0	8
‘05:53:19’	‘05:53:25’	0.260	0.472	-0.842	6.07	0.09	0.97	84.9	7
‘05:53:33’	‘05:53:39’	0.246	0.623	-0.743	10.46	0.03	0.89	88.1	7

Table 1 shows the components of the minimum variance directions in the VSO coordinate system, the intermediate-to-minimum eigenvalues ratio ($\lambda_{int}/\lambda_{min}$), the ratio of average magnetic field component along the minimum variance direction (B_n) to the larger field magnitudes on either side of the discontinuity ($|B_n|/|B|$), the ratio of the change of the field magnitude to the field magnitude ($|\triangle B|/|B|$), the angle between $|B_n|$ and $|B|$, $\theta\ _{B_n\_B}$ as well as the number of data points during the intervals analyzed.

The intermediate-to-minimum eigenvalues ($\lambda_{int}/\lambda_{min}$) of all 18 intervals are greater than 3.5 which implies that the minimum variance direction is well defined. All the $|B_n|/|B| <$ 0.14 (mean value of 0.06) and $|\triangle B|/|B| > 0.63$ (mean value of 0.86). These values are well within the criteria for tangential discontinuity; $|B_n|/|B| < 4$ and $|\triangle B|/|B| \geq 0.2$, indicating that this boundary represents a tangential discontinuity [*Knetter et al.*, 2004, and references therein]. In addition, all the angles between $|B_n|$ and $|B|$, $\theta_{B_n\_B} > 81.8°$ (mean value of 86.5°) which is approximately 90° further indicating all of the nine intervals of photoelectron dropouts are bounded by tangential discontinuities, a typical characteristic of the Venusian ionopause [*Wolff et al.*, 1980].

The same approach is applied to all the dip-to-peak and peak-to-dip field fluctuations immediately adjacent to the intervals of photoelectron dropout identified across the full data set. Note that field magnitude in a magnetized ionosphere is similar to that observed in the magnetic barrier region, unlike for the unmagnetized case. Hence, for the orbits when photoelectron dropouts are observed, the dip-to-peak and peak-to-dip field fluctuations in a magnetized ionosphere cannot clearly be identified. This results in only 371 unique orbits (from a total of 495 events) selected for further analysis. In these 371 orbits, 1043 intervals of photoelectron dropouts are observed, hence 2086 field fluctuations. Since MV analysis is only valid with 3 or more data points, only 1633 field fluctuations (from a total of 2086) which have 6 or more data points are selected. Analysis conducted using more data points would result in smaller data sets, and less data points would result in a higher statistical uncertainty [*Sonnerup and Scheible*, 1998]. The resulting distributions of the boundary normal directions are similar using between 3 and 9 data points. The use of a minimum of 6 data points is chosen as a compromise between the number of data sets and the statistical uncertainty.

Around 98% (1603 out of 1633 intervals) of all the minimum variance directions have $|B_n|/|B| < 0.4$ and $|\triangle B|/|B| \geq 0.2$, indicating boundaries of tangential discontinuity.

Similarly, around 95% (1562 out of 1633 intervals) have $\theta_{B_n\_B} > 75°$ further indicating that the analyzed intervals are tangential discontinuities. This is again consistent with the characteristics of the Venusian ionopause [*Wolff et al.*, 1980]. Furthermore, more than 88% (1446 out of 1633 intervals) have $\lambda_{int}/\lambda_{min} \geq 3$, which shows that the minimum variance directions are well defined. These results imply that the multiple photoelectron dropout events observed during each of these orbits, are due to VEX traversing the ionospheric boundary multiple times. For example on 02 Oct 2011, VEX traversed through the ionospheric boundary 9 times on a single trajectory.

Moreover, the dip-to-peak and peak-to-dip field fluctuations occur on the time scale of a few seconds. Since the decay of the magnetic field in the ionosphere is on a timescale from minutes to several hours [*Luhmann et al.*, 1984], the possible scenario of VEX traveled through patches of magnetized and unmagnetized regions of the ionosphere consecutively can be ruled out.

3.3 Ionospheric boundary waves

In addition to the previous analysis, a total of 251 VEX passes with ionospheric boundary crossings that are similar to the case presented on 08 Nov 2011 (no photoelectron dropout) are collected. The criteria used to select these passes were (1) no observations of photoelectron dropout events, (2) only gradual ionospheric crossings without magnetic intermediary and (3) clear passes from high field magnetic barrier to low field unmagnetized ionosphere. Results of MV analysis of the ionospheric boundary show that the minimum variance directions are very well defined with more than 96% (242 out of 251) of the directions having $\lambda_{int}/\lambda_{min} \geq 3$. The results also suggest that the crossings are ionospheric boundary with more than 98% (247 out of 251) having $\theta_{B_n\_B} > 75°$ and around 100% (250 out of 251) having $|B_n|/|B| < 0.4$ and $|\triangle B|/|B| \geq 0.2$.

All of the normal directions for the 238 (out of 251) ionopause crossings with $\lambda_{int}/\lambda_{min} \geq 3$ and number of data points ≥ 6 are binned in a three dimensional polar statistical histogram with an azimuthal ϕ bin size of 7.5° and elevation α bin size of 3.75° in Figure 3(a). ϕ and α are the angles between the locational radial vector from the center of the planet and the X-Z $_{VSO}$ and X-Y $_{VSO}$ planes respectively. ϕ ranges from 0° to 360°. While α ranges from −90° (southern polar point) to +90° (northern polar point). The colorbar at the bottom of the histogram is the number of ionopause crossings in each bin.

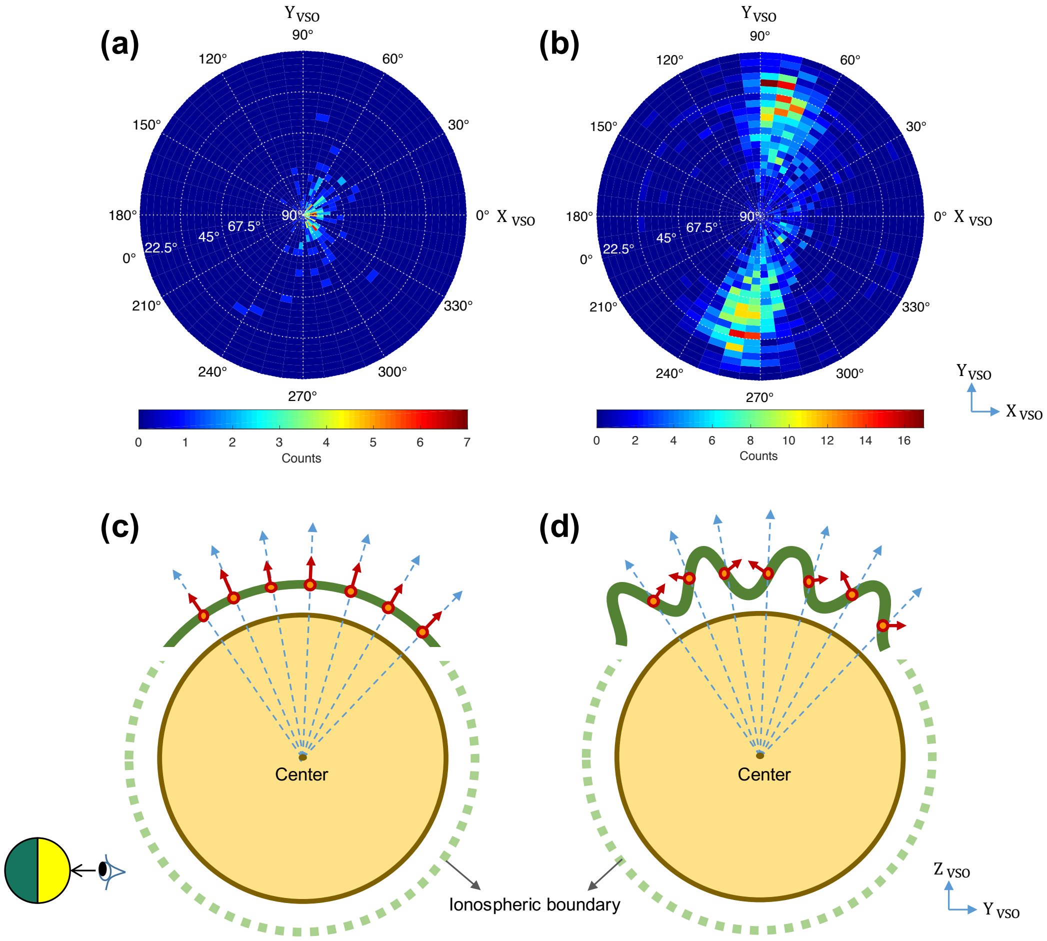

Figure 3. All of the normal directions of the ionospheric boundary crossings are binned in a three dimensional polar statistical histogram for ionospheric boundary crossing cases with (a) no observation of photoelectron dropout events as well as (b) observations of photoelectron dropout events with an azimuthal ϕ bin size of 7.5° and elevation α bin size of 3.75°. (a) and (b) are computed from a total of 238 and 1446 events respectively with criteria of $\lambda_{int}/\lambda_{min} \geq 3$ and number of data points ≥ 6. The colorbars at the bottom of the histograms are the number of ionopause crossings in each bin. Illustrative diagrams that show the projections of normal directions of ionospheric boundary crossings (especially in the northern polar regions where all of the boundary crossings are observed) for (c) a smooth ionospheric boundary and (d) an ionospheric boundary that exhibits a wavelike appearance. The green line represents the ionospheric boundary. The blue dashed arrows represent vectors projected radially from the center of Venus through its local locations. The red arrows represent the normal directions of the boundary crossings projected from their local locations which are denoted by the orange colored dots. Note that the illustration of the symmetric ionospheric boundary is visualized on the basis that the nominal ionopause altitude is not Solar Zenith Angle dependent [*Zhang et al.*, 2008b].

For ease of comparison, all minimum variance directions with negative Z_{VSO} components are rotated into the positive Z_{VSO} direction and the local positions of the boundary crossings are shifted to the northern polar point ($\alpha = 90°$) so that all directions can be visualized and compared in a single directional hemisphere. As seen in Figure 3(a), around 91% (217 out of 238) of the boundary normal directions fall in the elevation range of $\alpha > 67.5°$.

For a spherically smooth Venusian ionospheric boundary in the dayside and the polar regions as illustrated in Figure 3(c), the normal directions of boundary crossings should be aligned radially from the center of Venus at their local locations. This is reflected in the results in Figure 3(a). As the locations of boundary crossings are shifted to the northern polar region, the close proximity between the boundary normal directions and the radial directions (from the center of Figure 3(a)), implies that ionospheric boundary is smooth and quasi-spherical in the Y-Z $_{VSO}$ plane (i.e. Figure 3(c)).

However, this scenario of smooth Venusian ionospheric boundary is not reflected in the results obtained for the photoelectron dropout events. In Figure 3(b), all of the 1446 well defined boundary normal directions from the photoelectron dropout intervals are binned in a similar three dimensional polar statistical histogram. Figure 3(b) shows that the bins are more populated in the azimuthal range of $60° < \phi < 120°$ and $240° < \phi < 300°$ as well as in the elevation range of $\alpha < 45°$. In comparison to the smooth boundary case presented in Figure 3(a), only around 23% (333 out of 1446) of the boundary normal directions fall in the elevation range of $\alpha > 67.5°$. This shows that instead of pointing radially outward from the center of Venus, the majority of the normal directions of the boundary crossings lie in the Y-Z $_{VSO}$ plane, with the most dominant component along the Y_{VSO} axis. In contrast to Figure 3(a), the results from Figure 3(b) imply that, for a single orbital trajectory exhibiting multiple crossings of the ionospheric boundary, the ionopause crossings from the photoelectron dropout cases do not result from a smooth ionospheric boundary, but an ionospheric boundary that can exist as a ripple along the Y-Z $_{VSO}$ plane and which may propagate in a direction dominantly along the Y_{VSO} axis. This is illustrated in Figure 3(d). All the minimum variance directions are obtained from a variety of VEX trajectories with a range of azimuthal angles (not shown here), i.e. the result of consistent minimum variance directions shown here are not biased towards any particular VEX orbit.

3.3.1 Flux ropes

Crossings of magnetic flux ropes [*Russell and Elphic*, 1979; *Russell*, 1990; *Wolff et al.*, 1980] should be, in theory, in an idealized hydromagnetic state, similar to crossings of the Venusian ionospheric boundary. Both are tangential discontinuity boundaries [*Spreiter et al.*, 1970; *Wolff et al.*, 1979]. Based on its unique "potato chip" shaped hodogram as a key identifier [*Russell*, 1990], a total of 132 magnetic flux ropes resulting in 264 dip-to-peak and peak-to-dip field changes are identified in this statistical analysis. The second photoelectron dropout event on 02 Oct 2011 that corresponds to a dip-to-peak-to-dip field change from 05:48:41 to 05:48:55 is identified as a flux rope. The hodogram (with $\lambda_{int}/\lambda_{min} \approx 55$) has a "potato chip" shape as shown in Figure 4(a). In addition, the hodogram of the boundary crossing (with $\lambda_{int}/\lambda_{min} \approx 55$) from 05:47:56 to 05:48:09 (just before the flux rope is encountered) is shown in Figure 4(b). The start of both hodograms are marked with blue circles. In comparison to the "potato chip" shape hodogram in Figure 4(a), the hodogram shown in Figure 4(b) does not indicate field rotation and thus this is not a flux rope.

177 of these 264 dip-to-peak and peak-to-dip field changes have $\lambda_{int}/\lambda_{min} \geq 3$ and number of data points ≥ 6. Similar to Figure 3(b), the minimum variance directions of only the flux rope crossings as well as photoelectron dropout events excluding the flux ropes, are binned in a three dimensional polar histogram, with an azimuthal ϕ bin size of 7.5° and elevation α bin size of 3.75° in Figure 4(c) and Figure 4(d) respectively. Compared to the non flux rope cases in Figure 4(d), the boundary normal directions of the flux ropes in Figure 4(c) are slightly more randomly orientated. However, the majority of them can still be observed to lie along the Y_{VSO} axis.

In summary, the analysis of all the ionospheric boundary crossings from 2006 to 2014 reveals that the Venusian ionospheric boundary is not always smooth. In particular, 23% (495 orbits) of all the available orbits shows that the ionopause can often exhibits a wavelike appearance in the northern polar region, where all of the boundary crossings are observed. Figure 4(e) presents an illustrative diagram to show how the wavelike characteristic of the Venusian ionospheric boundary can be visualized from the simultaneous observations of photoelectron dropout events (top panel) and the changes in magnetic field magnitude (middle panel).

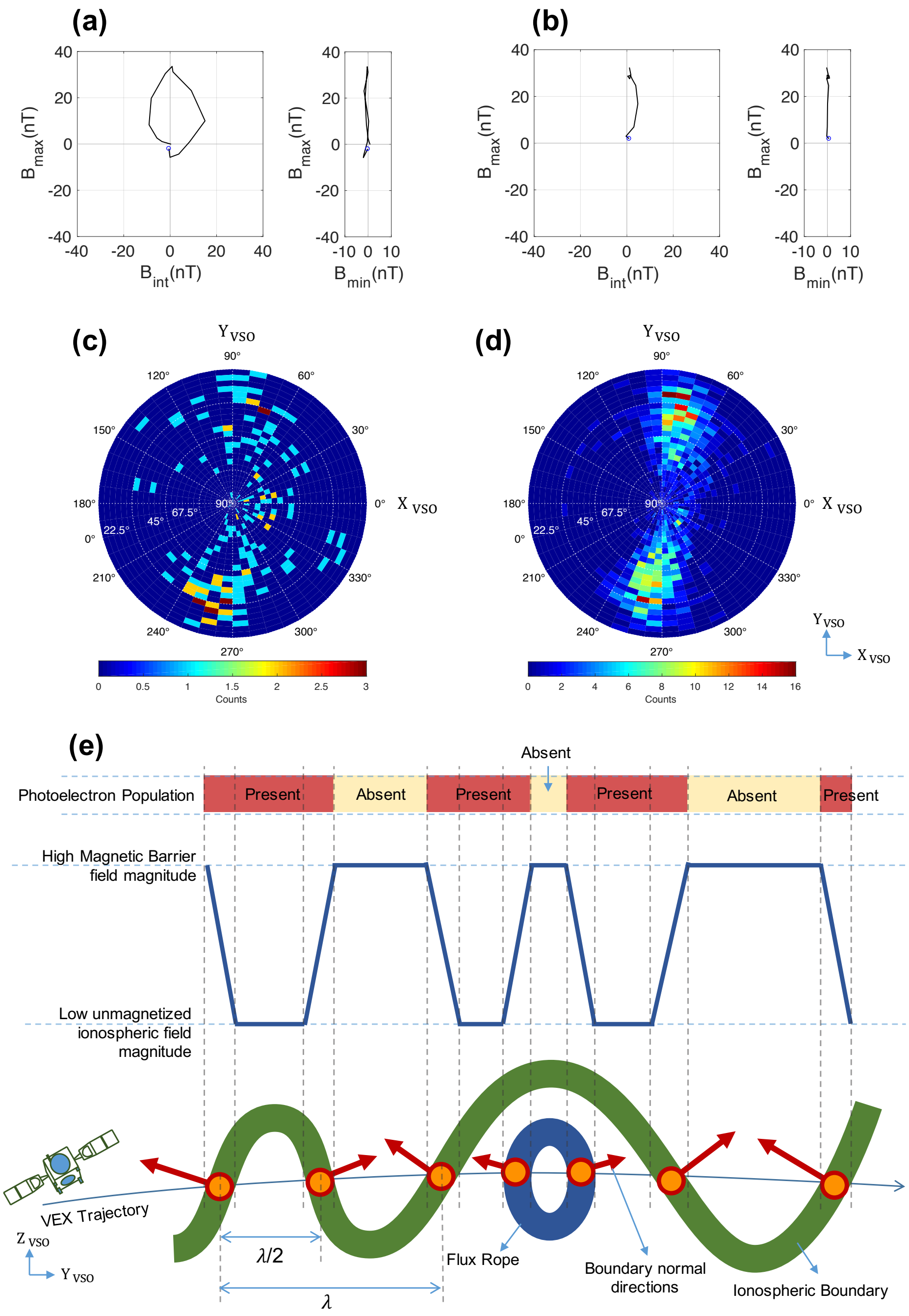

Figure 4. Hodogram of (a) a flux rope from 05:48:41 to 05:48:55 and (b) an ionospheric boundary crossing from 05:47:56 to 05:48:09 on 02 Oct 2011. All the normal directions of the boundary crossings are binned in a three dimensional polar histogram for ionospheric boundary crossings cases of (c) only flux ropes and (d) all photoelectron dropout intervals excluding flux ropes for comparison. (c) and (d) are computed from a total of 177 and 1269 events respectively. (e) An example illustrative diagram showing how the ionospheric photoelectron dropout events (top panel) and the changes in magnetic field magnitude (middle panel) can be related to the possible VEX trajectory through multiple ionospheric crossings and flux ropes (bottom panel). The red arrows represent the normal directions of boundary crossings projected from their local locations, which are denoted by the orange colored dots. λ and $\lambda/2$ denote estimated half-width and full width of the ionospheric boundary wave.

4 Discussions

Due to the polar orbit of VEX, the ionosphere is only sampled in the northern polar region, hence the ionospheric boundary wave events are observed in a rather small range of locations with elevation > 39° and with 90% of the observations made at > 61°. Its periapsis ranges from around 166 km to 1025 km, with 90% of the passes made below 475 km. The boundary wave events are observed everywhere in this small range of locations and do not show any particular preferred location.

4.1 Kelvin-Helmholtz Instability as a boundary wave generation mechanism

4.1.1 Boundary wave widths

With the assumption that the boundary wave is stationary with respect to the spacecraft velocity (VEX has velocity ~9.5 km/s around the periapsis), both the sizes of boundary wave billows and flux ropes can be estimated from the duration of their crossings along with their respective minimum variance orientation. The half-width of the boundary wave, $\lambda/2$ as illustrated in Figure 5(e) is estimated by the product of the VEX velocity and the time spent between two consecutive boundary crossings. The estimation is made under two criteria: (1) Only two consecutive boundary crossings when α_{mv}, the angle between their respective boundary normal directions, is less than 30° or greater than 150°, are selected to eliminate the crossings of boundary waves that are still in the linear growth phase; i.e. only developed waves are selected, (2) only boundary crossings when β_{vex}, the angle between the spacecraft velocity vector and the boundary normal vector is less than 45° are selected to eliminate the boundary crossings of the 'near-tips' of the waves as illustrated in Figure 5(e) and to eliminate the boundary which is crossed at a large angle by the VEX. These criteria yields a total of 89 boundary wave events. Note that the data of VEX, a single spacecraft mission, could only allow the estimations of the boundary normal directions but not the shape of the boundary wave. Hence the ionopause is expressed in a dashed line shaped question mark in the last (fourth) schematic diagram in Figure 5(e) indicating an undefinable shape. [*Brace et al.*, 1982]

A histogram of the estimated widths of the boundary wave λ, of the 89 events with a bin size of 50 km is presented in Figure 5(a). The distribution of the boundary wave widths is a single peak positively skewed distribution with a median value of 173 km and a mode class of 100-150 km. Mode class is the most frequent range of values in a dis-

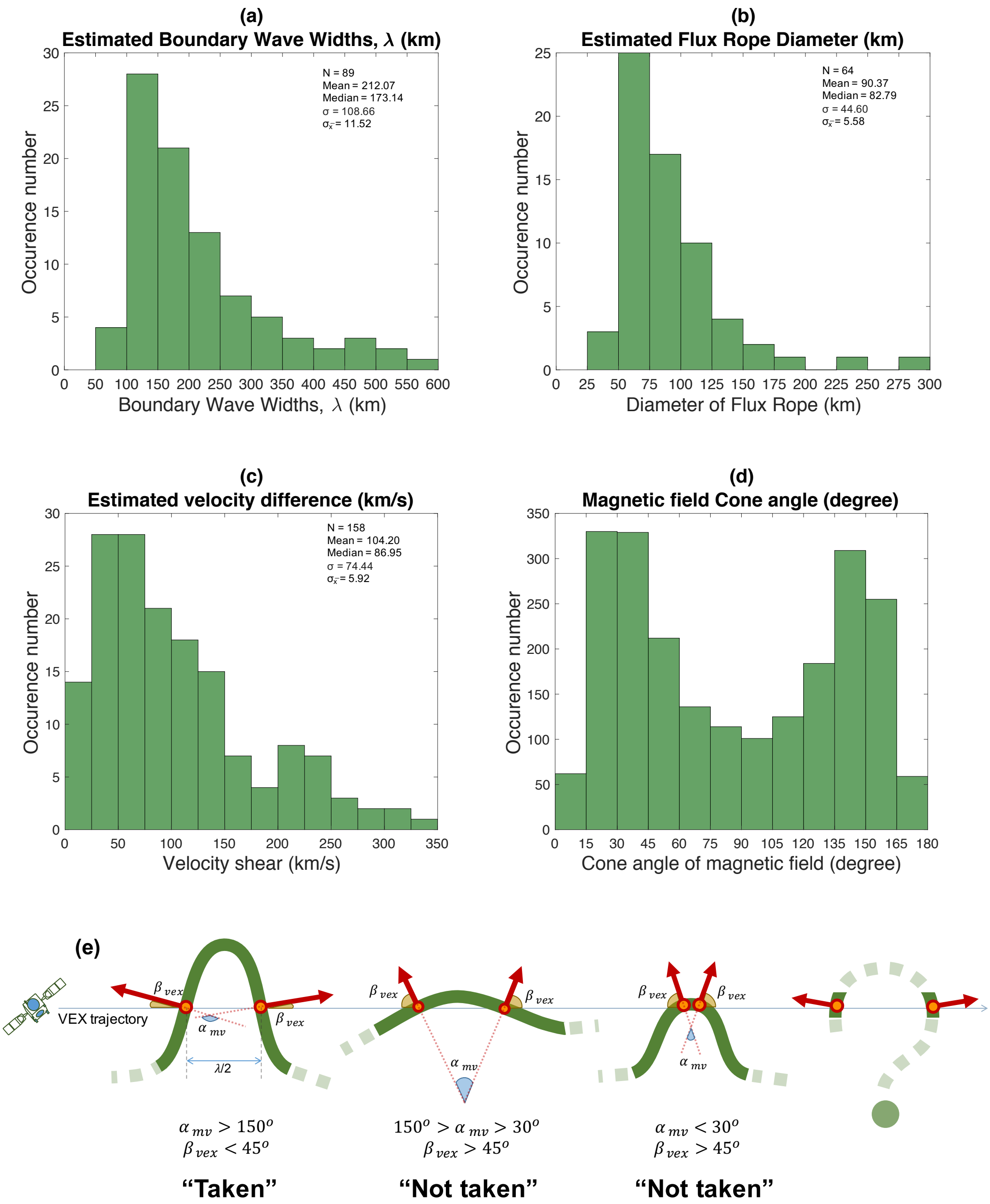

Figure 5. (a) A histogram of the estimated ionospheric boundary wave widths, λ from a total of 89 events from 2006 to 2014. Bin size is 50 km. Range: from 87 km to 550 km. (b) A histogram of the estimated flux rope diameter from a total of 64 events. Bin size is 25 km. Range: from 48 km to 295 km. (c) A histogram of the estimated velocity difference across the ionospheric boundary from a total of 158 events. Bin size is 25 km/s. Range: from 5 km/s to 341 km/s. (d) A histogram of the magnetic field cone angle in the magnetic barrier region from a total of 2216 events. Bin size is 15°. Cone angle is defined as $cos^{-1}(B_x/B)$. (e) Illustrative diagrams showing the criteria used in estimating the boundary wave widths and the flux rope diameter. The criteria are $\alpha_{mv} < 30°$ or $> 150°$ and $\beta_{vex} < 45°$. The red arrows represent the normal directions of boundary crossings projected from its local locations which are denoted by the orange colored dots. The ionospheric boundary is represented by green lines. β_{vex} is the angle between the spacecraft velocity vector and the boundary normal vector. α_{mv} is the angle between the boundary normal directions from two consecutive crossings.

tribution. It ranges from 87 km to 550 km and has an average width, λ of 212 ± 12 km. The lower 0.25 and higher 0.75 quantiles are 135 km and 255 km respectively. Additional analysis conducted with criterion $\beta_{vex} < 30°$ yields only 41 events but results in a similar average width, λ of 219 ± 17 km.

The diameters of the flux ropes are also estimated in a similar fashion but without the angle criteria mentioned earlier. Both of these criteria can be measured by the magnetic field magnitude along B_{min} of a flux rope crossing. For example, for a spacecraft to cross the exact center of a flux rope, the magnetic field magnitude along B_{min} should be zero. And for the case where the flux rope is not crossed through its center, there should be a finite non zero magnetic field magnitude along B_{min}. To measure the significance of the field magnitude along B_{min}, the $|B_{min}|/|B|$ value of all the flux ropes are calculated. In fact, the average value of $|B_{min}|/|B|$ for all the 133 flux ropes is only 0.12 ± 0.01. This indicates that all of the flux ropes observed were crossed at or very close to their center.

The estimated diameters of a total of 64 (out of 133) flux ropes which have $\lambda_{int}/\lambda_{min} \geq 3$ and number of data points ≥ 6 are presented in a histogram in Figure 5(b) with a bin size of 25 km. The distribution of the flux rope diameters is also a single peak positively skewed distribution with a median value of 83 km and a mode class of 50-75 km. It ranges from 48 km to 295 km and has an average diameter of 90 ± 6 km. The lower 0.25 and higher 0.75 quantiles are 59 km and 102 km respectively. Additional analysis conducted with criterion $\beta_{vex} < 45°$ yields a total of 25 flux ropes and an average diameter of of 79 ± 6 km. The low value of $|B_{min}|/|B|$ and the consistency shown in the estimated diameters regardless if the criterion on β_{vex} is applied, implies that the majority of the flux ropes are crossed quasi-radially and they do not appear to be ideally circular as depicted in Figure 4(e).

Note that if a boundary wave is configured similar to the three phases of the KHI evolution [*Amerstorfer et al.*, 2010], there are many possible ways that VEX can traverse through a boundary wave. Hence, with the limitations of the instruments on board of VEX, which is also a single spacecraft mission, estimations of the exact shape and thus the size of the observed boundary wave and flux ropes, are not possible.

4.1.2 Velocity shear profile

In addition to the estimation of boundary wave widths, the difference of velocity across the ionopause when boundary waves are observed, $|U_{iono} - U_{Mb}|$ is also calculated. U_{iono} and U_{Mb} are the average proton velocity in the ionosphere and magnetic barrier regions respectively. Due to the long IMA sampling time of 192s, to ensure there are at least two data points, only U_{iono} from orbits that VEX spent longer than 192s in the ionosphere are considered and U_{Mb} is estimated by taking an average proton velocity 5 minutes before crossing the inbound ionopause. A histogram of the measured velocity difference of 158 events with a bin size of 25 km/s is presented in Figure 5(c). The distribution of the velocity difference is a single peak positively skewed distribution with a median value of 87 km/s and a mode class of 25-75 km. The $|U_{iono} - U_{Mb}|$ ranges from 5 km/s to 341 km/s and has an average velocity of 104 ± 6 km/s.

Since the time spent by VEX in the magnetic barrier region is often short, much less than the long 192s sampling time of the IMA, the estimation of U_{Mb} by averaging the proton velocity 5 minutes before crossing the inbound ionopause, will often include the plasma populations in the sheath region. These have a much larger magnitude along the X_{VSO} axis due to the main solar wind bulk flow. Therefore, the U_{Mb} presented here is an overestimate and shows bias along the X_{VSO} axis. The magnitude of the 'actual' U_{Mb} is expected to be lower. Hence, the velocity difference profile presented here should be examined with caution.

In general, the results of the estimated ionospheric boundary wave widths and the velocity difference flow across the ionospheric boundary are considerably comparable with the study of KHI wave on Venus. For instance, *Wolff et al.* [1980] shows that with a 'gyroviscosity' coefficient, v_L of 250 km^2/s, a velocity difference of 100 km/s results in a wavelength of ~ 31 km while velocity difference of 10 km/s results in a wavelength of ~ 305 km. For a typical 30 km thin ionopause, *Elphic and Ershkovich* [1984] shows that velocity difference of 100 km/s and 200 km/s results in wave growth times of 81s and 32s respectively. Considering a density jump (ionosphere to the sheath region) with a ratio of 10, the local MHD simulation by *Amerstorfer et al.* [2010] with the lower (30 km) and upper (80 km) limits of ionopause boundary thickness [*Elphic et al.*, 1981], gives a dominant KHI wavelength with a lower range limit of ~181 km and a higher range limit of ~483 km. Similarly in *Ong and Roderick* [1972], for the most dominant mode of KHI, 30 km and 80 km of ionopause boundary thickness gives a dominant KHI wavelength with of ~224 km and ~600 km respectively. The comparable results shown between the estimated values in this statistical analysis and the simulation results, suggests that KHI may act as an excitation seed in inducing the ionospheric boundary wave that is observed in the northern polar region of Venus. However, it is noteworthy to mention that the average estimated ionospheric boundary wave width of 212 ± 12 km in this work lies close to the lower limit of *Amerstorfer et al.* [2010] and is actually 10 km smaller than the lower limit in *Ong and Roderick* [1972]. This slight inconsistency can be attributed to the different parameters (e.g. gyroviscosity, density gradient, and velocity difference etc.) considered in these mentioned studies which would result in different KHI wavelength.

Further analysis (not shown here) has been conducted to estimate the velocity difference of all orbits regardless of whether or not boundary waves are observed. The results show that the ionospheric boundary does not always exhibit a wavelike appearance when the velocity difference is large (i.e. $|U_{iono} - U_{Mb}| > 150$ km/s). This can be due to: (1) stabilizing terms (e.g. gravity [*Elphic and Ershkovich*, 1984]) which are more significant and dominate; (2) resolution of VEX data is too low to observe the short boundary wavelength resulting from the large velocity difference; and (3) the ionospheric boundary may exist in a wave but it is not traversed by VEX.

4.1.3 Orientation of magnetic field

Analysis reveals that the magnetic field orientation in the magnetic barrier region is quasi-perpendicular to the Y-Z $_{VSO}$ plane, which is a favorable condition for the excitation of KHI along the along the Y_{VSO} direction. This orientation is evidenced from the bimodal shaped distribution of the magnetic field cone angles in the magnetic barrier region presented in Figure 5(d), where the majority of the cone angles are < 45° and > 135°, i.e. quasi-parallel to the X_{VSO} axis. The distributions of the histogram are very consistent for all VEX passes regardless of whether boundary wave events are observed. This consistent quasi-parallel orientation of magnetic field lines to the X_{VSO} axis is due to the draping pattern of the magnetic field lines in the northern polar region of Venus. This is discussed further in the next section.

4.1.4 Impacts and consequences

When the KHI induced boundary wave becomes nonlinear, the broken wave can detach and form flux ropes, which transfers the shocked solar wind plasma in the ionosphere. The reconnection of the consecutive two troughs or two crests (i.e. $\lambda/2$) of a turbulent boundary wave would ideally result in the production of flux ropes with diameters comparable to the half-widths of the boundary wave. Therefore, the results of (1) the similarity in the normal directions between the flux ropes and the boundary wave (they mainly lie along the Y_{VSO} axis) and (2) the similarity between the estimated flux rope diameters and the half-widths ($\lambda/2$) of ionospheric boundary waves, suggest that the flux ropes observed are likely to be formed as a result of detached ionospheric boundary waves.

At the same time, atmospheric bubbles which contain plasma with ionospheric origin are also expected to form in a similar fashion to the production of flux ropes. Ideally, atmospheric bubbles can be identified by the observation of ionospheric photoelectron populations outside the ionosphere region. However, the convection of the atmospheric bubbles out of the ionosphere and subsequently downstream with the main solar wind bulk flow, can change the magnetization state as well as the characteristic energy signature of the ionospheric photoelectron populations (at 21-24eV and at 27eV [*Coates et al.*, 2008; *Cui et al.*, 2011]). In addition, the magnetic barrier region, where atmospheric bubbles populate before they are convected downstream, is highly dynamic. These complications may result in the atmospheric bubbles not being accurately identified in this work. On the other hand, the high latitude elliptical polar orbit of VEX indicates little opportunity for the spacecraft to encounter the atmospheric bubbles that often populate in the downstream region (-X_{VSO}) as a result of the convection of solar wind bulk flow.

4.2 Wave propagation along Y_{VSO}: Draping pattern of magnetic field lines

To assess if there is a preference in plasma velocity direction, the contribution of the average plasma velocity components along the X_{VSO}, Y_{VSO} and Z_{VSO} axes of the inbound solar wind (U_{sw}), magnetic barrier (U_{Mb}) and ionosphere (U_{iono}) are calculated. They are (91.3, 6.7, 2.1) % for the inbound solar wind, (75.2, 11.7, 13.2) % for the magnetic barrier and (15.1, 45.7, 39.2) % for the ionosphere. The values are normalized and are measured by taking the ratio of the individual components with respect to their overall magnitudes. They are expressed in percentage and the median values of their respective distributions are utilized for this calculations. To eliminate the possible orbital dependence of velocity, only quasi-terminator VEX trajectories are considered, i.e. when the orbital plane is < 30° to the terminator plane. The U_{sw}, U_{Mb} and U_{iono} are averaged from a total of 658, 341 and 465 plasma velocity vectors respectively.

Similar to Section 4.1.2, only U_{iono} from orbits for which VEX spent longer than 192s in the ionosphere are considered, while U_{sw} and U_{Mb} are estimated by taking an average of proton velocity 30 minutes before crossing the inbound bow shock and 5 minutes before crossing the inbound ionopause respectively. The results show that the average solar wind plasma velocity outside the bow shock is dominantly along the X_{VSO} axis, while the components along the Y_{VSO} and Z_{VSO} axes are minimal, as expected from the main solar wind bulk flow. However, through the bow shock and into the ionosphere, the contributions of the velocity component along the X_{VSO} axis can be observed to decrease drastically, while the contributions of the velocity components along the Y_{VSO} and Z_{VSO} axes becomes more significant. In the ionosphere, the plasma velocity is actually dominated by the components along the Y_{VSO} axis (with a contribution of $\approx$ 46%) followed by Z_{VSO} ($\approx$ 39%) and X_{VSO} ($\approx$ 15%) axes. These results are consistent with *Lundin et al.* [2011, 2013, 2014] in which the authors attributed the persistent $+Y_{VSO}$ directed ion flow over the northern polar region to the solar wind aberration.

The domination of the plasma velocity along the Y_{VSO} axis in the ionosphere region further suggests that a velocity shear profile across the ionospheric boundary could be set up and consequently exciting the boundary wave by means of KHI. However, the follow up question is: what is the possible driving mechanism of the plasma along the Y_{VSO} axis?

4.2.1 Dependence of the boundary normals with respect to their locations

Next the dependence of the normal directions of the boundary crossings with respect to their locations is studied. The MV_x, MV_y, and MV_z, which are the components of the normalized boundary normal directions along the X_{VSO}, Y_{VSO} and Z_{VSO} axes relative to the observation location of their associated boundary crossings in the X-Y_{VSO} plane are shown in Figure 6(a)-(c). The measurement for each normal direction is binned in 0.075×0.075 R_v bins ranging from -1 R_v to 1 R_v. Only bins with two or more measurements are shown.

The results presented in Figure 6(a)-(c) shows a clear dependence of the boundary normal directions on their respective locations, especially when the azimuthal angle of the locations, $\phi_{Location} < |45°|$. These regions are outlined with the black-colored dashed line which is just in front of X = 0. For instance, observable from Figure 6(a), the MV_x components in the region $\phi_{Location} < |45°|$ are much larger compared to the region $\phi_{Location} > |45°|$. This is visible by the stronger red-colored patches in the region outlined with the black-colored dashed line. In contrast, from Figure 6(b), the MV_y components in the same region are much smaller, visible from the weaker blue-colored patches. While MV_z components are rather randomly distributed. Even though the majority of the boundary normal directions are dominantly along the Y_{VSO} axis, the above results suggest that, at the location $\phi_{Location} < |45°|$, the boundary normal directions have slightly larger components along the X_{VSO} axis.

4.2.2 Draping of magnetic field lines

In Figure 6(d), taking the normal directions of the boundary crossings (represented as purple arrows) across an altitude range from 360 km to 370 km as an example, the boundaries (represented as red-dotted lines which are perpendicular to the normal directions) show an alignment that is comparable to a typical pattern of draped magnetic field lines (represented as blue lines) around Venus. These curved patterns are also valid at other altitude ranges (illustrations not shown here). The results from Figure 6(d) are consistent with Figure 6(a)-(c). The expected overall draping configuration of magnetic field lines across the cross section of altitude is illustrated in Figure 6(e).

Upstream of the bow shock, the IMF may appear in a range of orientations. The IMF moves towards Venus in the direction of the main solar wind bulk flow ($-X_{VSO}$). If the magnetic field lines are represented as an ellipse, as the field lines drape around the planet, the eccentricity tends from infinity (upstream of bow shock) towards zero (outside of the ionopause in the polar regions of Venus). This is illustrated in Figure 6(e) and (f). Typically, upstream of the bow shock, the solar wind has a higher plasma β (defined as the ratio of thermal to magnetic pressure). In this case, the thermal pressure dominates and the magnetic field lines are not “frozen into” the plasma. The plasma still gy-

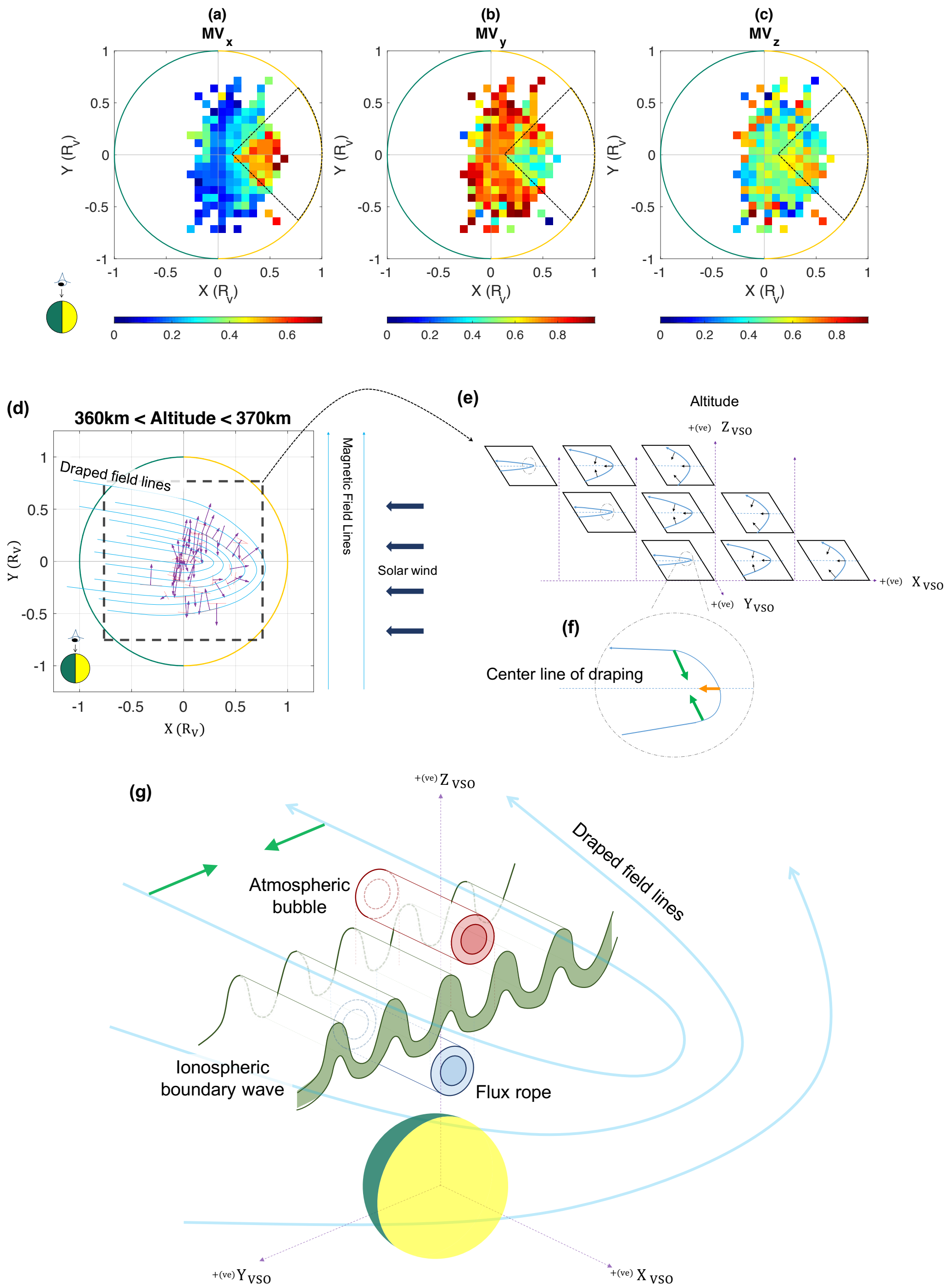

594 **Figure 6.** (a)-(c) The distribution of MV_x, MV_y, and MV_z, which are the components of the normalized
595 boundary normal directions along the X_{VSO}, Y_{VSO} and Z_{VSO} projected from their locations in the X-Y $_{VSO}$
596 plane. (d) An illustration of how all the perpendicular directions of boundary normal directions (from the
597 altitude band 360 km < altitude < 370 km) could be related to field draping. Note the intended slight solar
598 wind direction aberration is due to the orbital motion of Venus. (e)-(f) Illustrates how the draping patterns of
599 magnetic field lines may change as a function of altitude and along X_{VSO} direction for the area in the black
600 square box in (d) (adapted from [*Chong et al.*, 2017]). (g) Illustration of how field draping might lead to iono-
601 spheric boundary wave and the production of flux rope and atmospheric bubble. Illustration is not drawn to
602 scale.

rates around the field lines but has an overall velocity component mainly in the direction of solar wind bulk velocity in the $-X_{VSO}$ direction (represented by the orange arrow in Figure 6(f)). In contrast, through the magnetosheath the IMF lines start to pile up and drape around Venus more 'orderly and regularly', with the field lines eventually extending mainly in the direction of the solar wind bulk flow regardless of the IMF orientation [*McComas et al.*, 1986; *Masunaga et al.*, 2011; *Tanaka*, 1993]). At the same time, the plasma is slowly cooled down and slows towards the ionopause, where the thermal pressure is gradually converted into magnetic pressure. This consequently results in a lower β where the magnetic pressure dominates and the plasma is now "frozen into" the magnetic field lines. As a result, just outside of the Venusian ionopause around the polar regions, as illustrated by the green arrows in Figure 6(f), the now much lower β plasma is 'forced' to move towards the center line of draping (which is along the Y_{VSO} axis) due to the movement of magnetic field lines (which is along the Y_{VSO} axis). This could subsequently set up a velocity shear along the Y_{VSO} axis. In addition, as the density jump is along the Z_{VSO} axis in the northern polar region, the combination together with the velocity shear along the Y_{VSO} axis and the quasi-parallel orientation of magnetic field lines to the X_{VSO} axis, should favor the growth of KHI induced ionospheric boundary waves along the Y-Z $_{VSO}$ plane and with a propagation direction along the Y_{VSO} axis. This proposed mechanism is consistent with the results presented in this work and is illustrated in Figure 6(g). Note that the flux rope and the atmospheric bubble are only depicted simply to illustrate their possible presence. Their actual shapes are not known and the depicted circular shapes are for illustration purposes only.

The dependence of the boundary wave events on the orientations of the IMF has also been assessed. To eliminate the effects when the IMF might have changed between the inbound and outbound bow shock, IMF data is only considered when the angle between the inbound and outbound IMF orientations are $< 15°$. Results (not shown here) indicate that the IMF orientations for the orbits when ionospheric boundary wave events are observed and the orbits where they are not observed, are similar. This implies that the occurrence of boundary wave does not show any dependence on the orientations of the IMF.

5 Summary and conclusions

By utilizing the MAG, ELS and IMA data onboard of VEX, we have conducted the first statistical analysis of the perturbations of the ionospheric boundary at Venus over the period 2006 to 2014. Results from the minimum variance analysis reveals that the Venusian ionospheric boundary does not always appear to be smooth, but a rippled boundary that fluctuates mainly along the Y-Z $_{VSO}$ plane and predominantly with boundary normals along the Y_{VSO} axis. Further analysis shows that the estimated widths of the ionospheric boundary wave and the estimated velocity difference flow across the boundaries are consistent to the results from previous simulation studies of the Kelvin-Helmholtz Instability. This leads to the suggestion that the ionospheric boundary wave develops due to the Kelvin-Helmholtz Instability. Furthermore, our analysis suggests that the draping pattern of magnetic field lines play a principal role in enhancing the plasma flow along the Y_{VSO} axis and subsequently sets up a velocity shear that favors the excitation of ionospheric boundary waves.

When the Venusian ionospheric boundary is excited by the KHI and reaches a non-linear state, the wave can break off and detach, subsequently result in the formation of atmospheric bubbles and flux ropes. If ionopause waves [*Luhmann*, 1990] exist all along the terminator region, the draping pattern of magnetic field lines can act to enhance the production of both atmospheric bubbles and flux ropes, particularly in both the northern and southern polar regions of Venus where the magnetic field lines are more tightly draped. This can explain why the majority of the observed flux ropes from this statistical analysis, have similar widths and boundary normal directions to the ionospheric boundary wave. In addition, this scenario can also provide an explanation to the detection of atmospheric plasma outflows which are observed mainly in the polar regions; e.g. plasma clouds [*Brace et al.*, 1982] and high energy O^+ fluxes [*Masunaga et al.*, 2011]. Both studies attributed their respective observations to the limitations of the PVO orbits and the upstream IMF orientations. In addition, rippling ionopause could also potentially lead to the flapping of Venusian magnetotail [*Rong et al.*, 2015] and subsequently the productions of magnetic plasmoids in the magnetotail region [*Zhang et al.*, 2012]. However, since the ionosphere region is only sampled in locations limited to the northern polar region due to the polar orbit of VEX, it is not possible to assess and compare the nature of the ionospheric boundary in different regions, i.e. subsolar, southern polar and equatorial flank regions.

Continuous scattering and the subsequent convection of atmospheric bubbles downstream and away from Venus over a prolonged period of time plays an important role in atmospheric loss from Venus. The statistical analysis presented here, provides observational evidence of the ionospheric boundary existing in a wavelike appearance. This could have had a significant impact for the planetary evolution of Venus. However, the location of the boundary, which is a standoff boundary between the planetary atmosphere and the incoming solar wind, varies significantly depending on if the planetary body is magnetized. Hence, it is of interest for future work to measure the distributions of the boundary surface wave and assess the role of field draping on the stability of planetary boundaries, particularly for unmagnetized bodies where the boundaries are much closer to the planets.

Acknowledgments

Participants from Sheffield received financial assistance from STFC Consolidated Grant ST/R000697/1. Particle and low resolution magnetic field data are available from AMDA (http://amda.cdpp.eu/) and from the ESA Planetary System Archive (PSA) at https://www.cosmos.esa.int/web/psa/venus-express. High resolution MAG data is available on request from the VEX - MAG PI, Tie-Long Zhang. The authors would like to thank all the MAG and ASPERA-4 team members for the big effort which led to the successful operation of the instrument and the calibration of the data. R. Frahm acknowledges contributions from NASA (contract NASW-00003). The authors are very grateful for the insightful discussions with Glyn Collinson.

References

Amerstorfer, U. V., N. V. Erkaev, D. Langmayr, and H. K. Biernat (2007), On Kelvin-Helmholtz instability due to the solar wind interaction with unmagnetized planets, *Planetary and Space Science*, *55*(12), 1811–1816, doi:10.1016/j.pss.2007.01.015.

Amerstorfer, U. V., N. V. Erkaev, U. Taubenschuss, and H. K. Biernat (2010), Influence of a density increase on the evolution of the Kelvin-Helmholtz instability and vortices, *Physics of Plasmas*, *17*(7), 072901, doi:10.1063/1.3453705.

Arshukova, I., N. Erkaev, H. Biernat, and D. Vogl (2004), Interchange instability of the venusian ionopause, *Advances in Space Research*, *33*(2), 182–186, doi: 10.1016/j.asr.2003.04.015.

Barabash, S., J.-A. Sauvaud, H. Gunell, H. Andersson, A. Grigoriev, K. Brinkfeldt, M. Holmström, R. Lundin, M. Yamauchi, K. Asamura, et al. (2007), The analyser of space plasmas and energetic atoms (ASPERA-4) for the Venus Express mission, *Planetary and Space Science*, *55*(12), 1772–1792, doi:10.1016/j.pss.2007.01.014.

Biernat, H. K., N. V. Erkaev, U. V. Amerstorfer, T. Penz, and H. I. M. Lichtenegger (2007), Solar wind flow past Venus and its implications for the occurrence of the Kelvin-Helmholtz instability, *Planetary and Space Science*, *55*(12), 1793–1803, doi: 10.1016/j.pss.2007.01.006.

Brace, L. H., R. F. Theis, W. R. Hoegy, J. H. Wolfe, J. D. Mihalov, C. T. Russell, R. C. Elphic, and A. F. Nagy (1980), The dynamic behavior of the Venus ionosphere in response to solar wind interactions, *J. Geophys. Res.*, *85*(A13), 7663–7678, doi: 10.1029/JA085iA13p07663.

Brace, L. H., R. F. Theis, and W. R. Hoegy (1982), Plasma clouds above the ionopause of Venus and their implications, *Planetary and Space Science*, *30*(1), 29–37, doi: 10.1016/0032-0633(82)90069-1.

Brace, L. H., R. C. Elphic, S. A. Curtis, and C. T. Russell (1983), Wave structure in the Venus ionosphere downstream of the terminator, *Geophysical Research Letters*, *10*, 1116–1119, doi:10.1029/GL010i011p01116.

Chamberlain, J. W. (1963), Planetary coronae and atmospheric evaporation, *Planetary and Space Science*, *11*, 901–960, doi:10.1016/0032-0633(63)90122-3.

Chandrasekhar, S. (1961), *Hydrodynamic and Hydrodynamic stability*, OUP.

Chong, G. S., S. A. Pope, T. L. Zhang, G. A. Collinson, S. N. Walker, and M. A. Balikhin (2017), A study of ionopause perturbation and associated boundary wave formation at Venus, *Journal of Geophysical Research (Space Physics)*, *122*, 4284–4298, doi:10.1002/2016JA023769.

Coates, A. J., R. A. Frahm, D. R. Linder, D. O. Kataria, Y. Soobiah, G. Collinson, J. R. Sharber, J. D. Winningham, S. J. Jeffers, S. Barabash, J.-A. Sauvaud, R. Lundin, M. Holmström, Y. Futaana, M. Yamauchi, A. Grigoriev, H. Andersson, H. Gunell, A. Fedorov, J.-J. Thocaven, T. L. Zhang, W. Baumjohann, E. Kallio, H. Koskinen, J. U. Kozyra, M. W. Liemohn, Y. Ma, A. Galli, P. Wurz, P. Bochsler, D. Brain, E. C. Roelof, P. Brandt, N. Krupp, J. Woch, M. Fraenz, E. Dubinin, S. McKenna-Lawlor, S. Orsini, R. Cerulli-Irelli, A. Mura, A. Milillo, M. Maggi, C. C. Curtis, B. R. Sandel, K. C. Hsieh, K. Szego, A. Asamura, and M. Grande (2008), Ionospheric photoelectrons at Venus: Initial observations by ASPERA-4 ELS, *Planetary and Space Science*, *56*, 802–806, doi:10.1016/j.pss.2007.12.008.

Cui, J., M. Galand, A. J. Coates, T. L. Zhang, and I. C. F. Müller-Wodarg (2011), Suprathermal electron spectra in the Venus ionosphere, *Journal of Geophysical Research (Space Physics)*, *116*, A04321, doi:10.1029/2010JA016153.

Elphic, R. C., and A. I. Ershkovich (1984), On the stability of the ionopause of Venus, *J. Geophys. Res.*, *89*(A2), 997–1002, doi:10.1029/JA089iA02p00997.

Elphic, R. C., C. T. Russell, J. A. Slavin, and L. H. Brace (1980), Observations of the dayside ionopause and ionosphere of Venus, *J. Geophys. Res.*, *85*(A13), 7679–7696, doi: 10.1029/JA085iA13p07679.

Elphic, R. C., C. T. Russell, J. G. Luhmann, F. L. Scarf, and L. H. Brace (1981), The Venus ionopause current sheet - Thickness length scale and controlling factors, *Journal of Geophysical Research: Space Physics*, *86*, 11,430–11,438, doi: 10.1029/JA086iA13p11430.

Ferrari, A., S. Massaglia, and E. Trussoni (1982), Magnetohydrodynamic Kelvin-Helmholtz instabilities in astrophysics. III - Hydrodynamic flows with shear layers, *Monthly Notices of the Royal Astronomical Society*, *198*, 1065–1079.

Futaana, Y., G. Stenberg Wieser, S. Barabash, and J. G. Luhmann (2017), Solar Wind Interaction and Impact on the Venus Atmosphere, *Space Science Reviews*, *212*, 1453–1509, doi:10.1007/s11214-017-0362-8.

Hartle, R., and J. Grebowsky (1993), Light ion flow in the nightside ionosphere of venus, *Journal of Geophysical Research: Planets (1991–2012)*, *98*(E4), 7437–7445, doi: 10.1029/93JE00399.

Huba, J. D. (1981), The Kelvin-Helmholtz Instability in inhomogeneous plasmas, *J. Geophys. Res.*, *86*(A5), 3653–3656, doi:10.1029/JA086iA05p03653.

Jeans, J. H. (1955), *The dynamical theory of gases*, University Press.

Knetter, T., F. M. Neubauer, T. Horbury, and A. Balogh (2004), Four-point discontinuity observations using Cluster magnetic field data: A statistical survey, *Journal of Geophysical Research (Space Physics)*, *109*, A06102, doi:10.1029/2003JA010099.

Lammer, H., H. I. M. Lichtenegger, H. K. Biernat, N. V. Erkaev, I. L. Arshukova, C. Kolb, H. Gunell, A. Lukyanov, M. Holmstrom, S. Barabash, T. L. Zhang, and W. Baumjohann (2006), Loss of hydrogen and oxygen from the upper atmosphere of Venus, *Planetary and Space Science*, *54*(13-14), 1445–1456, doi: 10.1016/j.pss.2006.04.022.

Leinweber, H. K., C. T. Russell, K. Torkar, T. L. Zhang, and V. Angelopoulos (2008), An advanced approach to finding magnetometer zero levels in the interplanetary magnetic field, *Measurement Science and Technology*, *19*(5), 055104, doi:10.1088/0957-0233/19/5/055104.

Luhmann, J. G. (1990), 'Wave' analysis of Venus ionospheric flux ropes, *Washington DC American Geophysical Union Geophysical Monograph Series*, *58*, 425–432, doi:10.1029/GM058p0425.

Luhmann, J. G., and J. U. Kozyra (1991), Dayside pickup oxygen ion precipitation at Venus and Mars - Spatial distributions, energy deposition and consequences, *Journal of Geophysical Research: Space Physics*, *96*, 5457–5467, doi:10.1029/90JA01753.

Luhmann, J. G., and C. T. Russell (1997), Venus: Magnetic field and magnetosphere, in *Encyclopedia of Planetary Science*, Encyclopedia of Earth Science, pp. 905–907, Springer Netherlands.

Luhmann, J. G., C. T. Russell, and R. C. Elphic (1984), Time scales for the decay of induced large-scale magnetic fields in the Venus ionosphere, *Journal of Geophysical Research: Space Physics*, *89*, 362–368, doi:10.1029/JA089iA01p00362.

Lundin, R., S. Barabash, Y. Futaana, J.-A. Sauvaud, A. Fedorov, and H. Perez-de-Tejada (2011), Ion flow and momentum transfer in the Venus plasma environment, *Icarus*, *215*, 751–758, doi:10.1016/j.icarus.2011.06.034.

Lundin, R., S. Barabash, Y. Futaana, M. Holmström, H. Perez-De-Tejada, and J.-A. Sauvaud (2013), A large-scale flow vortex in the Venus plasma tail and its fluid dynamic interpretation, *Geophysical Research Letters*, *40*, 1273–1278, doi:10.1002/grl.50309.

Lundin, R., S. Barabash, Y. Futaana, M. Holmström, J.-A. Sauvaud, and A. Fedorov (2014), Solar wind-driven thermospheric winds over the Venus North Polar region, *Geophysical Research Letters*, *41*, 4413–4419, doi:10.1002/2014GL060605.

Masters, A., N. Achilleos, C. Bertucci, M. K. Dougherty, S. J. Kanani, C. S. Arridge, H. J. McAndrews, and A. J. Coates (2009), Surface waves on Saturn's dawn flank magnetopause driven by the Kelvin-Helmholtz instability, *Planetary and Space Science*, *57*, 1769–1778, doi:10.1016/j.pss.2009.02.010.

Masunaga, K., Y. Futaana, M. Yamauchi, S. Barabash, T. L. Zhang, A. O. Fedorov, N. Terada, and S. Okano (2011), O^+ outflow channels around Venus controlled by directions of the interplanetary magnetic field: Observations of high energy O^+ ions around the terminator, *Journal of Geophysical Research (Space Physics)*, *116*, A09326, doi:10.1029/2011JA016705.

McComas, D. J., H. E. Spence, C. T. Russell, and M. A. Saunders (1986), The average magnetic field draping and consistent plasma properties of the Venus magnetotail, *Journal of Geophysical Research: Space Physics*, *91*, 7939–7953, doi: 10.1029/JA091iA07p07939.

McElroy, M. B., M. J. Prather, and J. M. Rodriguez (1982), Loss of oxygen from Venus, *Geophysical Research Letters*, *9*, 649–651, doi: 10.1029/0GPRLA000009000006000649000001.

Möstl, U. V., N. V. Erkaev, M. Zellinger, H. Lammer, H. Gröller, H. K. Biernat, and D. Korovinskiy (2011), The Kelvin-Helmholtz instability at Venus: What is the unstable boundary?, *Icarus*, *216*, 476–484, doi:10.1016/j.icarus.2011.09.012.

Nykyri, K., and A. Otto (2001), Plasma transport at the magnetospheric boundary due to reconnection in Kelvin-Helmholtz vortices, *Geophysical research letters*, *28*, 3565–3568, doi:10.1029/2001GL013239.

Ong, R. S. B., and N. Roderick (1972), On the kelvin-Helmholtz instability of the Earth's magnetopause, *Planetary and Space Science*, *20*(1), 1–10, doi:10.1016/0032-0633(72)90135-3.

Penz, T., N. Erkaev, H. Biernat, H. Lammer, U. Amerstorfer, H. Gunell, E. Kallio, S. Barabash, S. Orsini, A. Milillo, et al. (2004), Ion loss on mars caused by the kelvin–helmholtz instability, *Planetary and Space Science*, *52*(13), 1157–1167, doi: 10.1016/j.pss.2004.06.001.

Pope, S. A., M. A. Balikhin, T. L. Zhang, A. O. Fedorov, M. Gedalin, and S. Barabash (2009), Giant vortices lead to ion escape from Venus and re-distribution of plasma in the ionosphere, *Geophys. Res. Lett.*, *36*(7), L07,202, doi:10.1029/2008GL036977.

Pope, S. A., T. L. Zhang, M. A. Balikhin, M. Delva, L. Hvizdos, K. Kudela, and A. P. Dimmock (2011), Exploring planetary magnetic environments using magnetically unclean spacecraft: a systems approach to VEX MAG data analysis, *Ann. Geophys.*, *29*(4), 639–647, doi:10.5194/angeo-29-639-2011.

Price, D. J. (2008), Modelling discontinuities and Kelvin-Helmholtz instabilities in SPH, *Journal of Computational Physics*, *227*(24), 10,040–10,057, doi: 10.1016/j.jcp.2008.08.011.

Rodriguez, J. M., M. J. Prather, and M. B. McElroy (1984), Hydrogen on Venus - Exospheric distribution and escape, *Planetary and space science*, *32*, 1235–1255, doi:10.1016/0032-0633(84)90067-9.

Rong, Z. J., S. Barabash, G. Stenberg, Y. Futaana, T. L. Zhang, W. X. Wan, Y. Wei, X. D. Wang, L. H. Chai, and J. Zhong (2015), The flapping motion of the Venusian magnetotail: Venus Express observations, *Journal of Geophysical Research (Space Physics)*, *120*, 5593–5602, doi:10.1002/2015JA021317.

Russell, C. T. (1986), The Venus magnetotail, *Advances in Space Research*, *6*, 291–300, doi:10.1016/0273-1177(86)90045-1.

Russell, C. T. (1990), Magnetic flux ropes in the ionosphere of Venus, *Washington DC American Geophysical Union Geophysical Monograph Series*, *58*, 413–423, doi:10.1029/GM058p0413.

Russell, C. T., and R. C. Elphic (1979), Observation of magnetic flux ropes in the Venus ionosphere, *Nature*, *279*(5714), 616–618, doi:10.1038/279616a0.

Russell, C. T., R. C. Elphic, and J. A. Slavin (1980), Limits on the possible intrinsic magnetic field of Venus, *J. Geophys. Res.*, *85*(A13), 8319–8332, doi:10.1029/JA085iA13p08319.

Sonnerup, B. U. Ö., and M. Scheible (1998), Minimum and Maximum Variance Analysis, *ISSI Scientific Reports Series*, *1*, 185–220.

Spreiter, J. R., A. L. Summers, and A. W. Rizzi (1970), Solar wind flow past nonmagnetic planets-Venus and Mars, *Planetary and Space Science*, *18*(9), 1281–1299, doi:10.1016/0032-0633(70)90139-X.

Sundberg, T., S. A. Boardsen, J. A. Slavin, L. G. Blomberg, and H. Korth (2010), The Kelvin-Helmholtz instability at Mercury: An assessment, *Planetary and Space Science*, *58*, 1434–1441, doi:10.1016/j.pss.2010.06.008.

Svedhem, H., D. V. Titov, F. W. Taylor, and O. Witasse (2007a), Venus as a more Earth-like planet, *Nature*, *450*(7170), 629–632, doi:10.1038/nature06432.

Svedhem, H., D. V. Titov, D. McCoy, J. P. Lebreton, S. Barabash, J. L. Bertaux, P. Drossart, V. Formisano, B. Häusler, O. Korablev, W. J. Markiewicz, D. Nevejans, M. Pätzold, G. Piccioni, T. L. Zhang, F. W. Taylor, E. Lellouch, D. Koschny, O. Witasse, H. Eggel, M. Warhaut, A. Accomazzo, J. Rodriguez-Canabal, J. Fabrega, T. Schirmann, A. Clochet, and M. Coradini (2007b), Venus Express-The first European mission to Venus, *Planetary and Space Science*, *55*(12), 1636–1652, doi:

10.1016/j.pss.2007.01.013.

Tanaka, T. (1993), Configurations of the solar wind flow and magnetic field around the planets with no magnetic field: Calculation by a new MHD simulation scheme, *Journal of Geophysical Research: Space Physics*, *98*, 17,251–17,262, doi:10.1029/93JA01516.

Terada, N., S. Machida, and H. Shinagawa (2002), Global hybrid simulation of the Kelvin-Helmholtz instability at the Venus ionopause, *J. Geophys. Res.*, *107*(A12), 1471, doi: 10.1029/2001JA009224.

Thomas, V. A., and D. Winske (1991), Kinetic simulation of the Kelvin-Helmholtz instability at the Venus ionopause, *Geophysical research letters*, *18*, 1943–1946, doi: 10.1029/91GL02552.

Titov, D. V., H. Svedhem, D. Koschny, R. Hoofs, S. Barabash, J. L. Bertaux, P. Drossart, V. Formisano, B. Häusler, O. Korablev, W. J. Markiewicz, D. Nevejans, M. Pätzold, G. Piccioni, T. L. Zhang, D. Merritt, O. Witasse, J. Zender, A. Accomazzo, M. Sweeney, D. Trillard, M. Janvier, and A. Clochet (2006), Venus Express science planning, *Planetary and Space Science*, *54*(13-14), 1279–1297, doi: 10.1016/j.pss.2006.04.017.

Walker, S. N., M. A. Balikhin, T. L. Zhang, M. E. Gedalin, S. A. Pope, A. P. Dimmock, and A. O. Fedorov (2011), Unusual nonlinear waves in the Venusian magnetosheath, *J. Geophys. Res.*, *116*(A1), A01,215, doi:10.1029/2010JA015916.

Wolff, R., B. Goldstein, and S. Kumar (1979), A model of the variability of the venus ionopause altitude, *Geophysical Research Letters*, *6*(5), 353–356, doi: 10.1029/GL006i005p00353.

Wolff, R. S., B. E. Goldstein, and C. M. Yeates (1980), The onset and development of Kelvin-Helmholtz instability at the Venus ionopause, *J. Geophys. Res.*, *85*(A13), 7697–7707, doi:10.1029/JA085iA13p07697.

Zhang, T. L., W. Baumjohann, M. Delva, H.-U. Auster, A. Balogh, C. T. Russell, S. Barabash, M. Balikhin, G. Berghofer, H. K. Biernat, H. Lammer, H. Lichtenegger, W. Magnes, R. Nakamura, T. Penz, K. Schwingenschuh, Z. Vörös, W. Zambelli, K.-H. Fornacon, K.-H. Glassmeier, I. Richter, C. Carr, K. Kudela, J. K. Shi, H. Zhao, U. Motschmann, and J.-P. Lebreton (2006), Magnetic field investigation of the Venus plasma environment: Expected new results from Venus Express, *Planetary and Space Science*, *54*, 1336–1343, doi:10.1016/j.pss.2006.04.018.

Zhang, T. L., M. Delva, W. Baumjohann, M. Volwerk, C. T. Russell, S. Barabash, M. Balikhin, S. Pope, K. H. Glassmeier, K. Kudela, C. Wang, Z. Vörös, and W. Zambelli (2008a), Initial Venus Express magnetic field observations of the Venus bow shock location at solar minimum, *Planetary and Space Science*, *56*(6), 785–789, doi: 10.1016/j.pss.2007.09.012.

Zhang, T. L., M. Delva, W. Baumjohann, M. Volwerk, C. T. Russell, S. Barabash, M. Balikhin, S. Pope, K. H. Glassmeier, C. Wang, and K. Kudela (2008b), Initial Venus Express magnetic field observations of the magnetic barrier at solar minimum, *Planetary and Space Science*, *56*(6), 790–795, doi:10.1016/j.pss.2007.10.013.

Zhang, T. L., Q. M. Lu, W. Baumjohann, C. T. Russell, A. Fedorov, S. Barabash, A. J. Coates, A. M. Du, J. B. Cao, R. Nakamura, W. L. Teh, R. S. Wang, X. K. Dou, S. Wang, K. H. Glassmeier, H. U. Auster, and M. Balikhin (2012), Magnetic Reconnection in the Near Venusian Magnetotail, *Science*, *336*, 567, doi:10.1126/science.1217013.